Near-threshold spectrum of photoelectron angular distributions from maximally oriented Ca $4s5p\,^1P$

K. W. McLaughlin, K. Aflatooni, and D. W. Duquette
Behlen Laboratory of Physics, University of Nebraska, Lincoln, Nebraska 68588-0111
(Received 27 September 1996; revised manuscript received 23 January 1997)

Photoelectron angular distributions from Ca $4s5p\,^1P$, maximally oriented using circularly polarized pulsed laser excitation, have been measured by rotating the linear polarization axis of a counterpropagating ionizing laser pulse. The angular distributions were measured as a function of ionizing energy in the near-threshold region encompassing the $3d4d\,^3D$ and ^3S autoionizing resonances as well as the newly identified ^1P resonance of the same configuration. Isotropic angular distributions in the vicinity of the new resonance is consistent with its total angular momentum $J=1$ assignment. Remote from the resonances, the ratio of the dipole matrix elements for photoelectron s- to d-wave production is independent of ionizing energy, while the relative phase difference between these partial waves varies significantly. An interference between partial waves gives rise to a previously unobserved asymmetry in the photoelectron angular distributions which is shown to occur within an independent-particle model. [S1050-2947(97)06505-0]

PACS number(s): 32.80.Dz, 32.80.Fb

I. INTRODUCTION

The near-threshold photoionization spectrum is known for displaying qualitative [1], as well as quantitative [2], deviations from independent-particle behavior. Photoelectron angular distributions provide some of the most detailed information for investigating these deviations since the interference between the photoelectron partial waves is preserved. The narrow energy resolution and polarization selectivity afforded by laser excitation allows atomic states to be prepared with well-defined energy, angular momentum, and magnetic substate population. Subtle details can be probed through studies from such well-defined states. Smith and coworkers [3] were the first to study configuration mixing in laser-excited states by taking advantage of the sensitivity of photoelectron angular distributions.

Berry and co-workers pioneered [4] the study of photoelectron angular distributions from excited states and were the first [5] to observe ''quantum beats'' or oscillations in these distributions due to the coherent superposition of hyperfine levels in the intermediate state. This hyperfine-induced mixing of magnetic sublevels was later found to be the mechanism by which nondipole allowed autoionizing levels were being excited in the photoionizing spectra from the $6s6p\,^1P$ [6] and $5d6p\,^3D_1$ [7] states of barium and the $3d^3\,^2D_{3/2}$ [8] state of scandium.

The presence of autoionizing resonances in the photoionization spectrum is a direct consequence of configuration interaction between the excited discrete state and the underlying continuum. In addition to aiding the assignment of spectroscopic symmetries for such resonances [9], angular distributions can be a sensitive probe of photoelectron dynamics within these regions [10]. Angular distributions can undergo dramatic changes as the ionizing energy is scanned through the resonance region [11]. Reaction-matrix multichannel quantum-defect calculations have been successful in reproducing [12] the complicated angular distribution spectra in the region of the $3pnd$ and $3pns$ autoionizing Rydberg states of magnesium, but less successful with the comparable $4pns$ states of calcium [13], the $5pns$ states of strontium [14], or the $6pns$ states of barium [15]. A modified R-matrix calculation has been extended recently to account for the angular distribution from inner-shell photoionization of excited atoms [16].

The total cross section for photoionizing the $4s5p\,^1P$ excited state of calcium has been measured recently in the near-threshold region encompassing the triplet S and D resonances of the $3d4d$ configuration [17]. In addition to these previously known terms, a new, extremely strong resonance, tentatively assigned as the ^1P term of the same configuration, was profiled at a resolution of 0.15 cm^{-1}. We report here measurements of photoelectron angular distributions as a function of ionizing energy encompassing these resonances. In addition to the photoelectron dynamics to be gleaned from such distributions, these measurements allow an independent assessment of the total angular momentum assignment of the newly identified resonance.

II. EXPERIMENTAL METHODS

A. Laser system and optics

The partial energy-level [18] diagram of Fig. 1 shows the relevant transitions pertaining to the present measurements. A frequency-doubled dye laser pulse excited ground-state calcium in an atomic beam to the $4s5p\,^1P$ state. A second, independently tunable, dye laser pulse selectively ionized this excited state with ionizing wavelengths from 668 to 695 nm. The resulting ionization energy range encompasses the doubly excited $3d4d\,^3S$ and ^3D terms and the recently identified [17] ^1P term of the same configuration. The ground state $Ca^+\ 4s\,^2S$ is the only accessible ionic channel for this ionizing energy range.

Photoelectron cross sections were put on a relative scale by normalizing the photoelectron yield to the fluorescence from the Ca $4s5p\,^1P \rightarrow 4s3d\,^1D$ transition at 672 nm. This line is sufficiently distinct from the excitation wavelength to

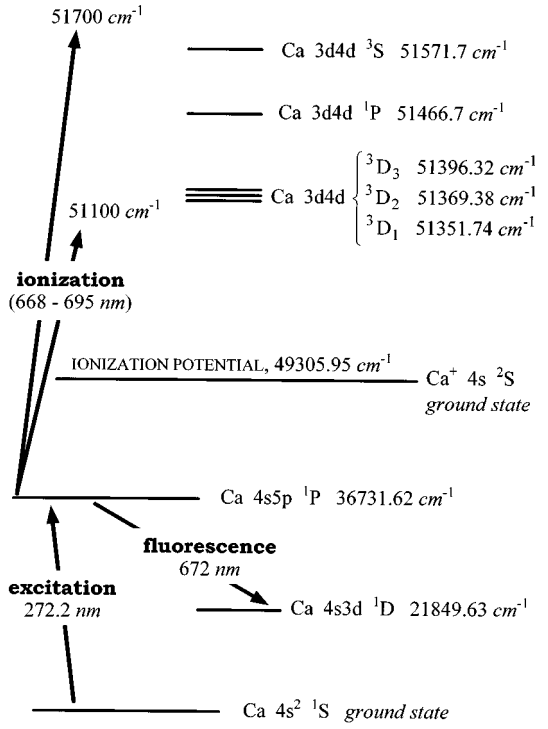

FIG. 1. Partial energy-level diagram of calcium illustrating the pertinent transitions used to assess relative photoionization cross sections from excited Ca $4s5p\,^1P$.

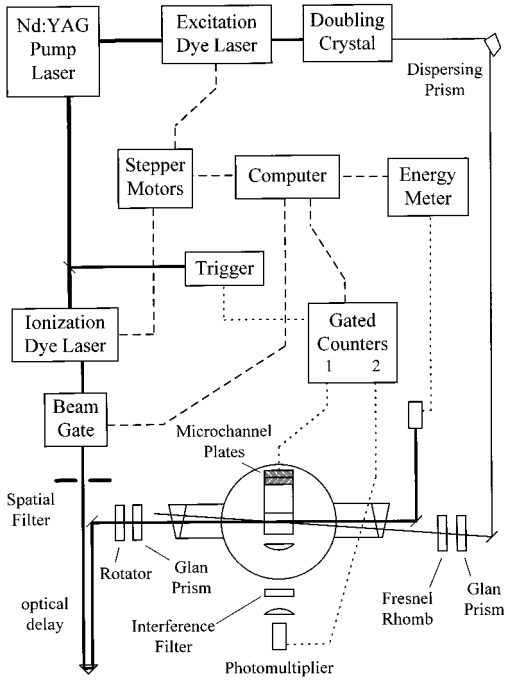

FIG. 2. Schematic of the overall experiment for assessing photoelectron angular distributions from oriented Ca $4s5p\,^1P$. Laser beams are indicated by solid lines, computer interfacing by dashed lines, and electrical signals by dotted lines.

allow the scattered light from the excitation laser pulse to be rejected from this measurement with a 30 nm bandwidth interference filter. With the presence of the ionizing laser pulse, however, scattered light prevented a reliable assessment of this fluorescence. Hence, the relative cross sections reported here could not be placed on an absolute scale by a method based on fluorescence depletion due to ionization [19].

Figure 2 shows a schematic of the overall experiment. Two independently tunable dye laser oscillators and associated amplifiers are pumped by a neodymium yttrium aluminum garnet (Nd:YAG) pulsed laser operating at a 10 Hz repetition rate. For clarity, the amplifier trains for the dye lasers are not shown. Both dye lasers are tuned by computer-controlled rotation stages. The output from the excitation dye laser, with a spectral linewidth $\leqslant 0.1\ \mathrm{cm}^{-1}$, is amplified twice and then frequency-doubled in a β-barium borate crystal. Following this frequency conversion, a Pellin-Broca dispersing prism diverts any remaining fundamental component from the subsequent beam path.

The outputs from both dye lasers are linearly polarized. The excitation beam is made circularly polarized using a Fresnel rhomb just prior to its entrance into the vacuum chamber. A Glan prism with a 10^5 extinction ratio ensures the purity of the linearly polarized radiation incident on this rhomb. The output from the ionization dye laser, with a spectral linewidth $\leqslant 0.15\ \mathrm{cm}^{-1}$, is amplified once, twice, or three times depending on the ionizing intensity required. A computer-controlled beam gate repetitively blocks the ionizing beam allowing the background photoelectron signal to be assessed along with the fluorescence from the excited state.

Following the beam gate, a 0.5 mm diameter aperture acts as a spatial filter for the ionizing beam. This increases the divergence such that the first diffraction minimum has a distinct diameter of 8 mm at the entrance to the vacuum chamber. A second iris with this diameter passes only the central maximum into the vacuum system. The diameter of the excitation beam upon entrance to the vacuum chamber is 1.5 mm. Thus, by aligning the center of the ionizing beam to overlap the excitation beam, the excited atoms are exposed to a pulse of ionizing radiation which, to a good approximation, is spatially uniform.

The outputs from both dye lasers are pulses of ≈ 5 ns duration. The ionizing pulse is delayed ≈ 15 ns relative to the excitation pulse by requiring the former to traverse a longer beam path. This assures that the excitation and ionizing transitions are sequential, independent processes.

A double Fresnel rhomb acts as an achromatic half-wave plate, allowing the linear polarization axis of the ionization beam to be rotated about its propagation axis without loss of intensity. A Glan prism polarizer following the double Fresnel rhomb was rotated to pass the output from the rhomb. This ensures the purity of the linear polarization state of the ionization beam to within the 10^5 extinction coefficient of the polarizer.

The two laser beams counterpropagate within the vacuum chamber with a divergence of $<0.5°$. The pulse energy of the ionizing beam was measured as this beam exited the vacuum chamber. The relative photoionization cross section was obtained by normalizing the photoelectron signal to this ionizing photon flux as well as the excited-state fluorescence.

B. Atomic source and detector systems

A schematic of the interior of the vacuum system has been published [17] and only a brief discussion is given here.

The calcium atomic beam is produced thermally by a thermocoax heater with the temperature monitored by an internal thermocouple embedded at the midpoint of the heating element. A reentrant nozzle terminates in a 45° chamfer to form an uncollimated atomic beam in an ''outer'' vacuum chamber. The atomic-beam nozzle is aligned 1.3 cm from the 2 mm diameter aperture which provides the coupling between the differentially pumped inner and outer vacuum chambers.

The oven temperature ranged between 790 to 830 K and was controlled to within ± 2 K. This corresponds to an atomic density of $\approx 1\times 10^{9}$ cm^{-3} at the center of the interaction region. This estimate assumes a saturated vapor expanded into a hemisphere upon exiting the nozzle and accounts for the canal factor [20] of $4d/3l = 0.16$, where l ($=0.53$ in.) is the channel length of the nozzle and d ($=1.6$ mm) is its diameter. At these densities radiation trapping of the observed fluorescence is completely negligible [21].

The interaction region and electron detection system within the inner vacuum chamber is magnetically shielded by 1 mm thick μ metal and electrically shielded with 60% transparent molybdenum (Mo) mesh. Using a Hall probe the magnetic field within the interaction region was found to be $\leqslant 4$ μT. The interaction region is within a hollow copper cylinder. Its endcaps consist of two electrically isolated copper ring electrodes 1.2 cm apart. The ring electrode in the direction of the photoelectron detector supports a Mo disk with a 3.6-mm-diam aperture resulting in a 0.28 sr solid angle acceptance for photoelectron detection.

The fluorescence collection system consisted of a photomultiplier coupled to the interaction region by two $f/2.5$ lenses. Photoelectrons are detected by dual microchannel plates in a chevron arrangement. The detectors have a common detection axis which is perpendicular to the plane defined by the atomic and laser beams. A drift region of 10 cm total length permits photoelectrons to be coarsely energy resolved by time of flight. The electrical isolation of the individual endcaps and cylinder of the interaction region allow an arbitrary bias potential to be placed across the interaction region. To collect all of the photoelectrons, the near endcap (relative to the drift region), cylinder, and far endcap electrodes were set at -30, -50, and -70 V, respectively. The -30 V near endcap potential, relative to the grounded entrance mesh of the drift region, serves to focus photoelectrons leaving the interaction region toward the microchannel plate detector. For angular-resolved measurements all electrodes are set at -50 V. This maintains the focusing at the entrance to the drift region while the interaction region is field free.

C. Data acquisition

The timing signal for the gated counter is obtained from a fast photodiode (1 ns rise time) detecting a reflection from the pump-laser beam. With the excitation laser tuned to the Ca $4s^2\ ^1S \rightarrow 4s5p\ ^1P$ transition and the ionizing radiation blocked and then unblocked, the count rates averaged up to 0.4 fluorescent photons and 0.1 photoelectrons per laser pulse, respectively. The cross section, with a standard deviation of $\leqslant 20\%$, was independent of ionizing photon flux for such count rates. The ionizing photon flux could be coarsely adjusted by removing amplification stages for this laser.

With the excitation laser detuned from the Ca $4s^2\ ^1S \rightarrow 4s5p\ ^1P$ transition, the photon and electron count rates dropped over two orders of magnitude from the average signal rates given above. Repetitive tuning and detuning was accomplished with the stepper-motor control of the excitation dye laser. The wavelengths of either dye laser output, measured with a monochromator, were linear with stepper-motor position over the tuning range of a dye (typically 30 nm) encompassing $11-12\times 10^{3}$ discrete steps of the stepper motor. Thus, the excitation dye laser could be reproducibly tuned with only its linewidth limiting the repeatability. With similar stepper-motor control of the ionizing dye laser, the discrete steps in the ionizing spectrum have a precision limited only by the 0.15 cm^{-1} linewidth of this laser. The absolute scale in the ionizing energy was limited by the ± 0.06 nm spectral resolution of the 24 cm focal length monochromator. After calibration with low-pressure discharge lamps, the observed line centers of the ^3S and $^3D_{1,2}$ resonances in the spectra were within ± 1 cm^{-1} of their previously assigned [18] positions. No further absolute wavelength determination was attempted.

Data acquisition was controlled via computer interfacing with the gated counter, ionizing beam gate, pulse energy meter, and the stepper motors controlling the tuning of both dye lasers. After a 20 s dwell time (200 laser pulses), the computer tuned or detuned the excitation laser for the Ca $4s^2\ ^1S \rightarrow 4s5p\ ^1P$ transition or gates the ionizing beam. Thus, photon and electron counts were accumulated both with and without the production of excited atoms, as well as with the ionizing radiation blocked and unblocked. These different permutations allowed background signals to be subtracted. With the wavelength of the ionizing laser beam fixed, each photoelectron angular distribution is the composite of angular differential cross sections measured sequentially.

III. DATA ANALYSIS

A. Angular distributions

Figure 3 defines a coordinate system for data analysis. The linear polarization axis and the propagation direction of the ionizing beam define the x axis and the $\hat{\mathbf{z}}$ direction, respectively. The polarization axis is referenced from the vertical atomic beam axis by the angle ϕ. This angle is obtained from a rotation stage which rotates the double Fresnel rhomb with a relative precision of $\pm 2°$. The electron detection axis is horizontal within the vacuum system. Hence, the photoelectron detection angle is $\varphi_e = \Phi - \phi$ with $\Phi \approx 90°$. Any misalignment in Φ, the angle between the reference for the rotation stage and the electron detection axis, represents a systematic error. An independent assessment of this error will be discussed in Sec. III B.

Figure 4 shows a polar plot of a photoelectron angular distribution. There is no classical interpretation for the tilt from the symmetry axis set by the linear polarization axis of the ionizing laser. This asymmetry results from the interference of photoelectron partial waves and will be discussed in Sec. IV B.

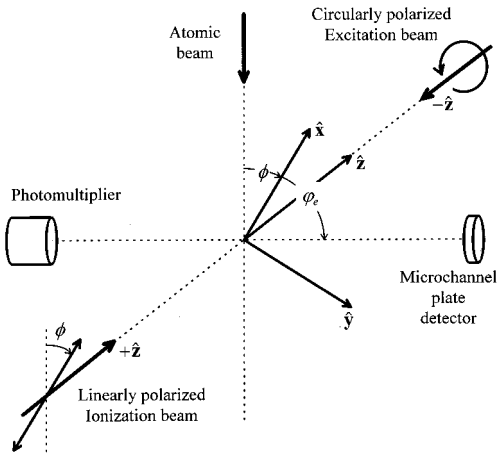

FIG. 3. Coordinate frame used for analysis of photoelectron angular distributions. The linear polarization axis and the propagation direction of the ionizing beam define the x axis and $\hat{\mathbf{z}}$ direction, respectively. The linear polarization axis is referenced from the atomic-beam axis by the angle ϕ. The photoelectron detection angle is $\varphi_e = \Phi - \phi$, with $\Phi \approx 90°$.

The polar plots must display an inversion symmetry due to the $\varphi_e + 180° \rightarrow \varphi_e$ invariance of Fig. 3. This symmetry was verified in initial measurements, but thereafter angle-differential measurements were only assessed from $\varphi_e = 90°$ to $-90°$. To aid visualization, the experimental data are duplicated and inverted through the origin in the polar plots.

The solid line in Fig. 4 corresponds to the expression (after accounting for finite angular acceptance)

$$\left.\frac{d\sigma}{d\Omega}\right|_{\theta_e=\pi/2} = a + b\cos(2\varphi_e) + c\sin(2\varphi_e). \tag{1}$$

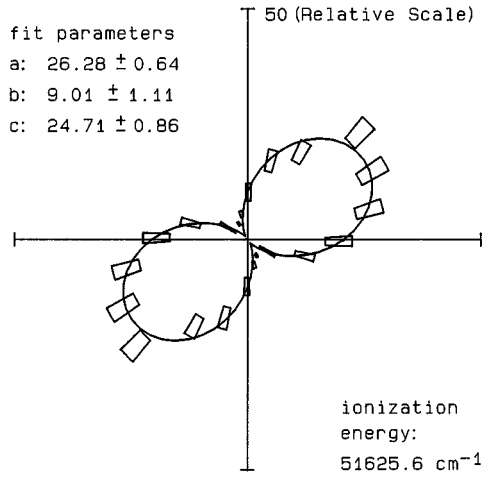

FIG. 4. Polar plot of the azimuthal photoelectron angular distribution from oriented Ca $4s5p\ ^1P$. The width and radial dimensions of the wedged boxes indicate the uncertainty in the detection angle and the cross section, respectively. The detection angle φ_e of Fig. 3 is referenced counterclockwise from the x axis of the polar plot. The ionization energy is relative to the Ca $4s^2\ ^1S$ ground state. The solid line denotes the fit to Eq. (3).

The physical significance of this form and its parameters will be discussed shortly. The fit parameters a, b, and c were estimated by minimizing χ^2 defined [22] by

$$\chi^2 \equiv \sum_{i=1}^{N} \left[\frac{\sigma_{\text{pred}}(\varphi_i) - \sigma_{\text{obs}}(\varphi_i)}{s(\varphi_i)}\right]^2, \tag{2}$$

where $\sigma_{\text{obs}}(\varphi_i)$ and $s(\varphi_i)$ represent the observed angle-differential cross section and its standard deviation at the photoelectron detection angle φ_i. The subscript e denoting the photoelectron is dropped here for clarity. N is the total number of data points in the angular distribution measurement. The minimization of χ^2 was accomplished using an iterative Gauss-Newton technique [23].

To account for the finite angular acceptance for photoelectron detection

$$\begin{aligned}\sigma_{\text{pred}}(\varphi_e) &= \int_{\varphi_e-\Theta}^{\varphi_e+\Theta} d\varphi_e' \left.\frac{d\sigma}{d\Omega}\right|_{\theta_e=\pi/2} \\ &= 2a\Theta + \frac{b}{2}\left[\sin(2\varphi_e+2\Theta) - \sin(2\varphi_e-2\Theta)\right] \\ &\quad - \frac{c}{2}\left[\cos(2\varphi_e+2\Theta) - \cos(2\varphi_e-2\Theta)\right],\end{aligned} \tag{3}$$

with the angular acceptance $2\Theta = 0.6$ rad. The angular distributions are not absolute measurements; therefore the relevant quantities are the ratios b/a and c/a. These ratios for the parameters of Eq. (3) differed by less than one standard deviation from the corresponding ratios for the parameters of Eq. (1). Thus this correction for the finite angular acceptance had a minor influence on the results. Since the expansion is in terms of orthogonal functions, the fit parameters are uncorrelated and the standard deviation Δ_b for the coefficient b is given [24] by

$$\Delta_b^2 = 2\left[\frac{\partial^2}{\partial b^2}(\chi^2)\right]^{-1}, \tag{4}$$

with similar expressions for the other two parameters.

B. Diagnostic experiments

A possible source of systematic error in the photoelectron detection angle φ_e involved Φ, the angle between the reference for the rotation stage and the electron detection axis. This alignment could be established to within $\pm 2°$. An assessment of any systematic error was made as follows. If the handedness of the circularly polarized excitation is reversed, the angular distribution must display a mirror reflection about the plane defined by the laser propagation and the electron detection axes (the *detection plane*). The handedness of the circularly polarized excitation was reversed by interchanging the ''fast'' and ''slow'' axes of the Fresnel rhomb. The resulting angular distribution of Fig. 5 displays the expected reflection about the $\varphi_e = 0$ axis of the polar plot. A correction of $\Phi \rightarrow 90° - 1.1°$ was required in order that the tilt for the two patterns exactly mirror one another through this axis. This source of systematic error was eliminated by applying this correction to all angular distributions.

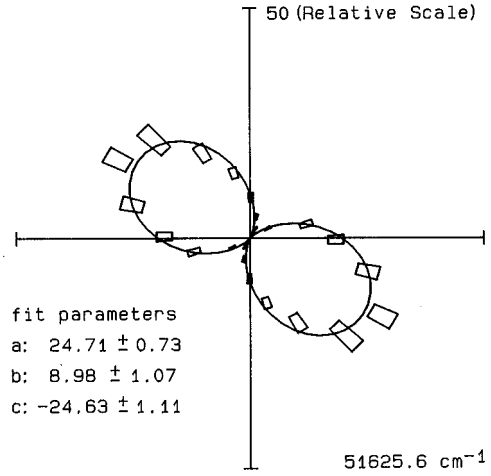

FIG. 5. Azimuthal distribution of photoelectrons from Ca $4s5p\,^1P$ oriented with circularly polarized excitation of the opposite handedness relative to the angular distribution of Fig. 4.

To further assess this correction independently, Fig. 6 shows the angular distribution using linear rather than circularly polarized excitation. With the linear polarization axis of the excitation beam fixed along the atomic beam axis, the angular distribution must be invariant to a reflection through the *detection plane*. This follows from Fig. 3 since the photoelectron detection is symmetric about the detection axis. Combining this symmetry with the $\varphi_e+180°\rightarrow\varphi_e$ inversion invariance, the polar plot must also display a reflection symmetry about the plane of polarization for the excitation beam (the $\varphi_e=90°$ axis in the polar plot). Using method [25] to be discussed shortly, the theoretical distribution for this case is given by

$$\left.\frac{d\sigma}{d\Omega}\right|_{\theta_e=\pi/2}=a_0+a_2\cos(2\varphi_e)+a_4\cos(4\varphi_e). \tag{5}$$

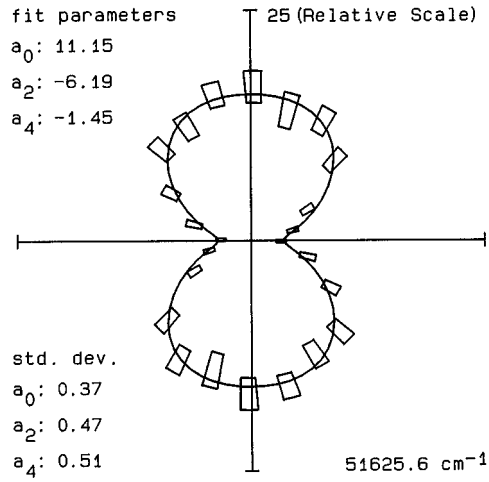

FIG. 6. Angular distribution of photoelectrons from laser aligned Ca $4s5p\,^1P$. With the linear polarization axis of the excitation beam fixed, the distribution is obtained by rotating the linear polarization axis of the counterpropagating ionizing laser. The solid line denotes the fit to Eq. (5) after accounting for finite angular acceptance.

The solid line in Fig. 6 corresponds to this expression (after accounting for finite angular acceptance) with the a_n fit parameters listed in the figure. Any asymmetry for this distribution can be investigated by fitting the distribution of Fig. 6 to

$$\left.\frac{d\sigma}{d\Omega}\right|_{\theta_e=\pi/2}=a_0+a_2\cos(2\varphi_e)+b_2\sin(2\varphi_e)+a_4\cos(4\varphi_e)+b_4\sin(4\varphi_e). \tag{6}$$

This latter fit resulted in $b_2=-0.38\pm0.61$ and $b_4=-0.40\pm0.55$, with the a_n coefficients unchanged. *Without* the 1.1° correction applied to Φ, these coefficients were $b_2=-0.78\pm0.43$ and $b_4=-0.59\pm0.39$ and, therefore, are significantly different from zero. Thus, the minor 1.1° correction appears to eliminate the systematic misalignment.

Since the angular distributions are relative measurements, the pertinent experimental quantities are the ratios b/a and c/a for the anisotropic terms of Eq. (3). For the distribution of Fig. 4, these quantities are $b/a=0.343\pm0.043$ and $c/a=0.940\pm0.040$. The sensitivity of these results to the purity of the circular polarization state of the excitation beam was investigated by one further diagnostic experiment. In order to introduce an elliptical component into the polarization state of the excitation beam, the optical axis for the Fresnel rhomb was purposely misaligned by 10° from its

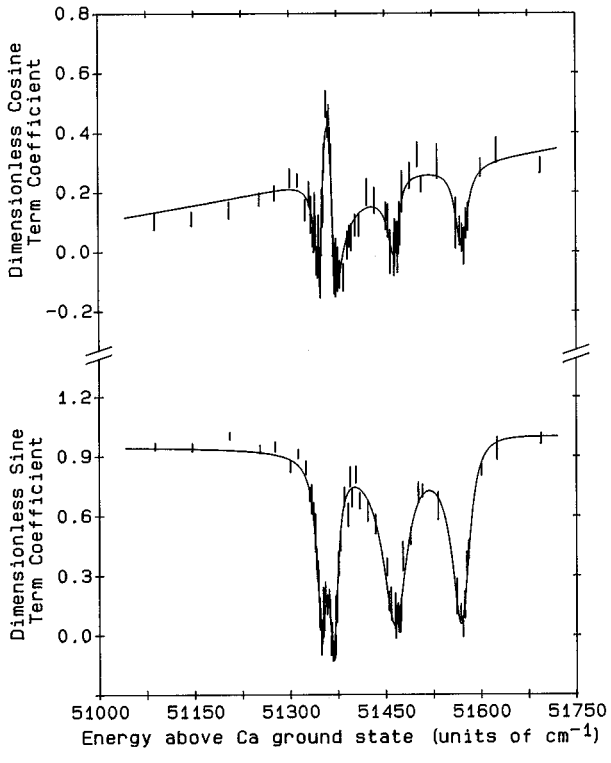

FIG. 7. The spectra for the anisotropic fit parameters of Eq. (3): (top) dimensionless cosine term coefficient b/a; (bottom) dimensionless sine term coefficient c/a. The vertical extent of each data box indicates a one standard deviation uncertainty. The solid line represents a sum of terms of the form of Eq. (7) for each resonance plus a linear background term. The fit parameters are given in Tables I and II.

TABLE I. Resonance parameters obtained by fitting the spectrum for the anisotropic cosine coefficient in Fig. 7 to a sum of profiles of the form of Eq. (7) plus a linear background term. The background continuum was fit to $A(E-51\,400\ \mathrm{cm}^{-1})+B$, with $A=3.52(\pm0.50)\times10^{-4}$ and $B=0.198\pm0.007$.

	Resonance energy E_0 (cm^{-1})	Width Γ (cm^{-1})	X	Y	Z
$^3D_1$	51 351.7	5.45 ± 0.45	$-2.27\ (\pm0.82)\times10^{-2}$	0.415 ± 0.060	-0.336 ± 0.026
$^3D_2$	51 369.4	8.21 ± 0.70	$6.15\ (\pm0.75)\times10^{-2}$	-0.426 ± 0.056	-0.264 ± 0.042
^1P	51 466.7	10.0 ± 2.3	statistically insign.	$9.7\ (\pm4.1)\times10^{-2}$	-0.241 ± 0.036
^3S	51 571.7	12.5 ± 3.4	$3.0\ (\pm2.2)\times10^{-3}$	$-7.0\ (\pm5.1)\times10^{-3}$	-0.300 ± 0.035

proper 45° alignment with the transmission axis of the Glan prism. The proper alignment could be established to within ±2°. The distribution with the imposed misalignment had the following fit parameters: $b/a=0.306\pm0.039$ and $c/a=0.891\pm0.035$. The small influence due to the imposed misalignment established that the uncertainty in the proper alignment was insignificant. This result further indicates that the pollution imposed on the polarization state of either laser beam by the windows to the vacuum chamber also had a negligible influence. The 3° wedged windows to the vacuum chamber were oriented such that the two faces were 1.5° from the vertical. The fractional excess between vertical and horizontal linear basis states transmitted into the vacuum chamber is three orders of magnitude less than that imposed by the 10° misalignment of the Fresnel rhomb.

IV. DISCUSSION OF RESULTS

A. Spectra

The spectra for the normalization parameter a in Eq. (3) and that for the total cross section were in excellent agreement with each other and with that previously reported [17]. Figure 7 shows the spectra of the anisotropic fit parameters in Eq. (3), expressed as the dimensionless ratios b/a and c/a. These spectra were fit to a sum of generalized [25,26] Fano-type profiles for each resonance

$$\frac{b}{a}\ \text{or}\ \frac{c}{a}=\frac{X\epsilon^2+Y\epsilon+Z}{1+\epsilon^2}. \tag{7}$$

X, Y, and Z are fit parameters with $\epsilon\equiv(E-E_0)/\Gamma$, the ionizing energy relative to the linewidth Γ and position E_0 of each resonance. These fit parameters, given in Tables I and II, were estimated by minimizing the appropriate χ^2 values. The total cross section varies by orders of magnitude in the vicinity of each resonance. However, the near vanishing of the anisotropic terms b/a and c/a at peak centers artificially *broadens* the peak widths in the spectra for these coefficients by *restricting* the peak depths to changes only on the order of unity. For this reason the resonance linewidths Γ for the anisotropic parameters, b/a and c/a, do not agree with those from the total cross-section measurement. The sum of isolated resonance profiles (7) provided an adequate fit to the spectra of Fig. 7 only if the resonance linewidths were treated as fit parameters as well.

The angular distributions changed dramatically within the vicinity of the $^3D_1$ and $^3D_2$ resonances at 51 352 and 51 369 cm^{-1}, respectively. Figure 8 displays the distributions in this region with the vertical arrangement qualitatively indicating the total cross section at the corresponding ionizing energy. The waist of the angular distribution pattern balloons with the pattern progressively changing its orientation as the $^3D_1$ resonance is approached from the low-energy side or the $^3D_2$ resonance is approached from the high-energy side. A progressive change in orientation continues in the vicinity between these two fine-structure levels. This change in orientation was not observed for the ^1P or ^3S resonances; the pattern simply became isotropic as these resonance positions were approached.

At peak center of the four resonances the sine-term coefficient c/a does not differ significantly from zero and the cosine-term coefficient b/a is nonzero only at the peak of the $^3D_2$ resonance. Thus the angular distributions are isotropic at peak center for those resonances with total angular momentum $J_r=1$.

A recently published [25] density matrix formalism is convenient for analyzing the current experimental results. An isotropic distribution is predicted [25,27] for linearly polarized dipole excitation to a strong $J_r=1$ resonance from an

TABLE II. Resonance parameters obtained by fitting the spectrum for the anisotropic sine coefficient in Fig. 7 to a sum of profiles of the form of Eq. (7) plus a linear background term. The background continuum was fit to $\alpha(E-51\,400\ \mathrm{cm}^{-1})+\beta$, with $\alpha=2.29(\pm1.17)\times10^{-5}$ and $\beta=0.976\pm0.007$.

	Resonance energy E_o (cm^{-1})	Width Γ (cm^{-1})	X	Y	Z
$^3D_1$	51 351.7	8.95 ± 0.42	$-1.48(\pm0.76)\times10^{-2}$	-0.111 ± 0.029	-0.716 ± 0.028
$^3D_2$	51 369.4	6.33 ± 0.36	$-7.2(\pm2.6)\times10^{-3}$	0.199 ± 0.034	-0.677 ± 0.025
^1P	51 466.7	25.0 ± 1.3	statistically insign.	0.167 ± 0.038	-0.880 ± 0.041
^3S	51 571.7	16.9 ± 1.6	$2.32(\pm0.59)\times10^{-2}$	0.231 ± 0.050	-0.891 ± 0.047

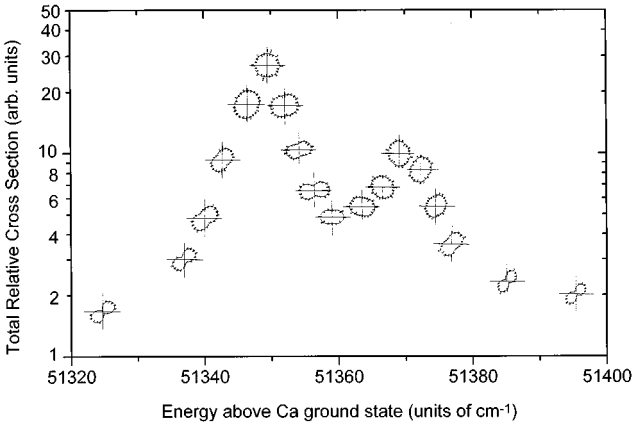

FIG. 8. Photoelectron angular distributions in the ionizing energy region encompassing the $^3D_1$ and $^3D_2$ resonances. The vertical arrangement corresponds qualitatively to the total relative cross section at the corresponding ionizing energy. (Note the logarithmic vertical scale.)

initial $J_0=1$ state which is maximally oriented ($M_0=+1$ or -1) along the propagation direction of the ionizing radiation. A $J_r=0$ resonance would likewise yield an isotropic distribution. Thus, the isotropic distribution observed in the vicinity of the new resonance at 51 467 cm^{-1} is consistent with either a $J_r=0$ or 1 assignment. However, only the $J_r=1$ assignment is consistent with previous observations [17,27].

Similarly, linearly polarized dipole excitation to a strong $J_r=2$ resonance from a maximally oriented $J_0=1$ initial state leads to distributions of the form of Eq. (1) where the sine-term coefficient vanishes [25,27]. This prediction can be justified without resorting to detailed angular-momentum coupling methods. Parity and total angular-momentum conservation considerations allow only the photoelectron d-wave contribution for the dipole excitation

$$\mathrm{Ca}\ \ 4s5p(J_0=1)+\gamma\rightarrow(J_r=2)\rightarrow \mathrm{Ca}^+\ \ 4s\ ^2S+e.$$

It is the interference between the photoelectron partial waves which gives rise to the tilt from the symmetry axis set by the linear polarization axis of the ionizing radiation. Thus, neglecting the continuum contribution, the angular distribution at peak center for the $^3D_2$ resonance is easily predicted to display no asymmetric tilt. The spectra of Fig. 7 and the two distributions of Fig. 8 in the vicinity of the peak of the $^3D_2$ resonance at 51 369.4 cm^{-1} support this prediction.

B. Angular distribution asymmetry

The conclusion that the interference between partial waves is the source of the tilt from the symmetry axis is easily shown for a hydrogenic p state. Within an electric dipole approximation and treating the interaction with the ionizing radiation to first order in perturbation theory, the photoelectron angular distribution is given by [28]

$$\frac{d\sigma}{d\Omega}=\frac{4\pi^2\omega}{c}\,k\left(\frac{me^2}{\hbar^2}\right)|\langle\Psi_k|\hat{\mathbf{e}}\cdot\vec{\mathbf{r}}|\Psi_0\rangle|^2, \tag{8}$$

where Ψ_0 and Ψ_k denote the initial and final state, respectively, with $\vec{\mathbf{r}}$ the electron coordinate and k the magnitude of the photoelectron wave vector. The ionizing photon has polarization $\hat{\mathbf{e}}$ and energy $\hbar\omega=E_b+(\hbar k)^2/2m$, where E_b denotes the binding energy of the ejected electron.

The final state in Eq. (8) should have the asymptotic boundary condition appropriate for photoionization which requires that as $t\rightarrow\infty$ a localized wave packet can be constructed with linear momentum $\hbar\vec{\mathbf{k}}$. For photoionization from a neutral atom the ejected electron experiences a long-range Coulomb potential resulting in the modified partial-wave expansion [28]

$$\Psi_k(\vec{\mathbf{r}})=k^{-1/2}\sum_{l=0}^{\infty}\sum_{m=-l}^{+l} i^l e^{-i(\sigma_l+\delta_l)}R_{El}(r)Y_{lm}(\hat{\mathbf{r}})Y^*_{lm}(\hat{\mathbf{k}}), \tag{9}$$

where the presence of a Coulomb phase shift σ_l along with the short-range interaction phase shift δ_l enters into the normalization factor for each term in the summation and the radial wave function $R_{El}(r)$ has the Coulomb logarithmic phase factor in its asymptotic form as well [28]. The spherical harmonic $Y^*_{lm}(\hat{\mathbf{k}})$ in the expansion (9) gives the amplitude for a photoelectron in this angular-momentum state to have the direction $\hat{\mathbf{k}}$.

For the coordinate system defined in Fig. 3 the ionizing radiation propagates along the quantization z axis for the polarized atom and the linear polarization axis of the ionizing beam defines the x axis. The angular distribution given by Eq. (8) with $\hat{\mathbf{e}}\cdot\vec{\mathbf{r}}=x$ can be written as

$$\frac{d\sigma}{d\Omega}=A_0|\langle\Psi_k|rY_{1,-1}(\hat{\mathbf{r}})-rY_{1,+1}(\hat{\mathbf{r}})|\Psi_0\rangle|^2, \tag{10}$$

with

$$A_0=\frac{4\pi^2\omega}{c}\,k\left(\frac{me^2}{\hbar^2}\right)\left(\frac{2\pi}{3}\right).$$

Substituting $\Psi_0(\mathbf{r})=R_{n,l'=1}(r)Y_{1,+1}(\hat{\mathbf{r}})$ for an initial hydrogenic p_{+1} state and the Coulomb partial-wave expansion (9) for the final-state results in

$$\frac{d\sigma}{d\Omega}=A_1|\xi_{00}e^{i\Delta_s}Y_{00}(\hat{\mathbf{k}})R_s-\xi_{20}e^{i\Delta_d}Y_{20}(\hat{\mathbf{k}})R_d+\xi_{22}e^{i\Delta_d}Y_{22}(\hat{\mathbf{k}})R_d|^2, \tag{11}$$

where $A_1=A_0/k$, $\Delta_l=\sigma_l+\delta_l$, and

$$R_l=\int dr\ r^3R_{El}(r)R_{n,l'=1}(r)\quad(l=s,d)$$

denotes the radial dipole matrix elements. The dipole selection rules ($\Delta l=\pm1$) arise from an integral over three spherical harmonics with the following numerical results: $\xi_{00}=-(4\pi)^{-1/2}$, $\xi_{20}=(20\pi)^{-1/2}$, and $\xi_{22}=(3/10\pi)^{1/2}$. Evaluating Eq. (11) in the azimuthal plane results in

TABLE III. The ratio R_s/R_d for the reduced dipole matrix elements for photoelectron s- to d-wave production and the relative phase difference $\Delta_d-\Delta_s$ between these matrix elements consistent with the photoelectron angular distributions from Ca $4s5p\ ^1P$.

Ionizing energy[b] (cm^{-1})	Propensity favored[a]		Propensity unfavored[a]	
	$\lvert R_s/R_d\rvert$	$(\Delta_d-\Delta_s)$[c]	$\lvert R_s/R_d\rvert$	$(\Delta_d-\Delta_s)$[c]
51 088	0.607 ± 0.025	$111.9°\pm3.5°$	2.49 ± 0.09	$90.5°\pm2.6°$
51 146	0.602 ± 0.031	$111.5°\pm2.2°$	2.50 ± 0.10	$89.8°\pm2.9°$
51 205	0.655 ± 0.026	$107.7°\pm3.5°$	2.23 ± 0.09	$89.3°\pm2.8°$
51 695	0.658 ± 0.041	$98.3°\pm3.6°$	2.03 ± 0.13	$81.4°\pm3.1°$

[a]Refers to the propensity for the electric dipole $l\rightarrow l+1$ photoabsorption to normally dominate over the $l\rightarrow l-1$ channel.

[b]Relative to the calcium ground state which has an ionization threshold of 49 305.95 cm^{-1}.

[c]The phase difference $\Delta\equiv\Delta_d-\Delta_s$ is modulo $2n\pi\pm\Delta$ with n an integer.

$$\left.\frac{1}{A_2}\frac{d\sigma}{d\Omega}\right|_{\theta_e=\pi/2}=c_1+\tfrac{3}{2}[\cos(2\varphi_e)-2R\cos(2\varphi_e+\Delta)]$$

$$=c_1+\tfrac{3}{2}c_2\cos(2\varphi_e-\eta) \tag{12}$$

using $\Delta=\Delta_d-\Delta_s$, $R=R_s/R_d$, $c_1=R^2-R\cos(\Delta)+\frac{5}{2}$, $c_2=1+4R^2-4R\cos(\Delta)$, $A_2=(\pi\omega m/6c)(eR_d/\hbar)^2$, and $\eta=\tau-\Delta/2$ with

$$\tan(\tau)=\left(\frac{1+2R}{1-2R}\right)\tan\left(\frac{\Delta}{2}\right).$$

Equation (12) can be rearranged to the form of Eq. (1) by a further trigonometric identity.

In the limiting case where the d wave dominates, $R=R_s/R_d\rightarrow0$ and the azimuthal distribution would display no asymmetric tilt from the linear polarization axis of the ionizing radiation. In the limit where the s wave dominates, it is easily predicted from Eq. (11) that the angular distribution is isotropic. For small relative phase shifts such that $\Delta\rightarrow0$, the azimuthal distribution again displays no tilt from the symmetry axis even for the case where both partial waves are significant. In general, it is a nonvanishing relative phase shift $\Delta=\Delta_d-\Delta_s$ that produces an asymmetric tilt of the azimuthal distribution from this axis. The magnitude of this tilt will vary when the relative strength R of the partial waves varies or when the relative phase shift Δ varies.

Resulting from an interference between partial waves this asymmetry has no classical interpretation. The observation of this asymmetry requires the system to be oriented. With both lasers linearly polarized, no asymmetry due to the interference of partial waves is observed. An asymmetry can be observed in the sense that the photoelectron trajectory favors the acute angle between the two polarization axes; however, this propensity has an obvious classical interpretation due to the force on the atomic oscillator [5,29]. If both photons had been circularly polarized there is no observable photoelectron angular variations in the azimuthal plane to the laser beam propagation. Therefore, in addition to a required orientation, one of the photons must be linearly polarized in order to provide a reference in this azimuthal plane. Angular displacements from this reference with the same handedness as the circularly polarized photon qualitatively differ from angular displacements made with the opposite handedness.

C. Atomic parameters

A recent density matrix formalism [25] is convenient for generalizing these hydrogenic results for the photoionization process: Ca $4s5p\ ^1P+\gamma\rightarrow Ca^+\ 4s\ ^2S+e(l,j)$ involving a maximally oriented initial state. Neglect of relativistic effects imposes the condition that $\Delta S=0$ and eliminates any dependence on the fine structure of the final state. The two experimental parameters b/a and c/a of Eq. (1) can then be written [25,27] in terms of two atomic parameters

$$\frac{a}{\zeta}=\frac{R^2}{6}+\frac{R\cos(\Delta)}{6\sqrt{10}}(\sqrt{2}+\sqrt{3})+\frac{299\sqrt{70}+48\sqrt{105}-140}{1260\sqrt{70}}, \tag{13a}$$

$$\frac{b}{\zeta}=\frac{R\cos(\Delta)}{2\sqrt{10}}(\sqrt{2}+\sqrt{3})+\frac{172\sqrt{3}+29\sqrt{2}}{1680\sqrt{2}}, \tag{13b}$$

and

$$\frac{c}{\zeta}=\frac{R\sin(\Delta)}{2\sqrt{10}}(\sqrt{2}+\sqrt{3}), \tag{13c}$$

where $R\equiv R_s/R_d$ is the ratio of the radial dipole matrix elements for the photoelectron s- to d-wave production and $\Delta\equiv\Delta_d-\Delta_s$ is their relative phase difference. In atomic units $\zeta=\pi\alpha\omega R_d^2$, with ω the ionizing photon energy and α the fine-structure constant.

Since Eqs. (13a)–(13c) are noninvertible, the solution for the atomic parameters consistent with the experimental quantities $(b/a)_{obs}$ and $(c/a)_{obs}$ was obtained by the following graphical technique for solving simultaneous equations. A contour plot using the ratios of Eq. (13) with the specified value $(b/a)=(b/a)_{obs}$ yields those values of R and Δ which are consistent with $(b/a)_{obs}$. Similarly, those values consistent with $(c/a)_{obs}$ are obtained from a contour plot with the specification $(c/a)=(c/a)_{obs}$. The intersection of these two contour plots yields the unique values of R and Δ consistent with both $(b/a)_{obs}$ and $(c/a)_{obs}$. Repeating this process with the standard deviations imposed on $(b/a)_{obs}$ and $(c/a)_{obs}$ allows the uncertainties in R and Δ to be estimated.

Since Eq. (13a) is quadratic in R there are two solutions consistent with $(b/a)_{obs}$ and $(c/a)_{obs}$. In Table III these so-

lutions are labeled according to the propensity for the electric dipole $l \rightarrow l+1$ photoabsorption to normally dominate over the $l \rightarrow l-1$ channel. Due to the sinusoidal dependence in Eq. (13) and the fact that the absolute handedness of the circularly polarized excitation photon was not determined, the phase difference is specified only within modulo $2n\pi \pm \Delta$ with n an integer. The ionizing energies considered in Table III are at the extremes of the ionizing energy region studied, sufficiently remote from the autoionizing regions such that the angular distributions exhibited no perturbation from these resonances.

There is one previous measurement with which our results can be compared. A photoelectron angular distribution from Ca $4s4p\,^1P$ has been measured [29] at a single ionizing energy of 53 314 cm^{-1} above the Ca ground state. The excitation and ionizing laser beams were both linearly polarized. With the relative angle between these two linear polarization axes fixed, the angular distribution was measured by rotating both linear polarization axes simultaneously. The theoretical expression involved an expansion of associated Legendre functions up to fourth order. The expansion coefficients yielded the following estimates: $|R| = 0.70 \pm 0.21$ and $|\cos(\Delta)| = 0.05 \pm 0.03$. Within the interval [0°,360°] there are four values of Δ consistent with these estimates, although the inequality $R\cos(\Delta) < 0$ was established [29]. The present propensity-favored values agree with this established sign.

Since the propensity-unfavored values are inconsistent with this previous measurement these solutions will no longer be considered physical. The propensity-favored values, however, are in excellent agreement with an improved precision for the assessment of $|R_s/R_d|$. This ratio shows an insignificant energy dependence over the ionizing energy region studied here. The mean value $|R_s/R_d|_{\text{avg}}$ of 0.63 plus or minus one standard deviation of 0.03 is consistent with all four reported values in Table III. In contrast, the relative phase difference $(\Delta_d - \Delta_s)$ varies significantly with ionizing energy even within the small region of the spectrum studied.

V. SUMMARY

Photoelectron angular distributions from Ca $4s5p\,^1P$, maximally oriented using circularly polarized pulsed laser excitation, have been measured by rotating the linear polarization axis of a counterpropagating ionizing laser pulse. The angular distributions were measured as a function of ionizing energy from 1800 to 2400 cm^{-1} above threshold. This near-threshold region encompasses the $3d4d\,^3D$ and ^3S autoionizing resonances as well as the newly identified ^1P resonance of the same configuration. An ionizing energy resolution of 0.15 cm^{-1} allowed the angular distribution spectrum within the $3d4d\,^3D_{1,2}$ fine structure to be clearly resolved. The spectra for the parameters describing the angular distributions were well fit by a sum of generalized Fano-type profiles for each resonance. In agreement with prediction, isotropic angular distributions were observed at peak center for each resonance with total angular momentum $J=1$. Isotropic distributions in the vicinity of the new resonance is consistent with its ^1P assignment.

Remote from the resonances, the ratio of the dipole matrix elements for photoelectron s- to d-wave production is 0.63 plus or minus one standard deviation of 0.03, independent of ionizing energy within the region of the spectrum studied. In contrast, the relative phase difference between these photoelectron partial waves varies significantly with ionizing energy. A nonclassical asymmetry was observed in the continuum photoelectron angular distributions. This asymmetry was shown to occur within an independent-particle model and arises from an interference between partial waves.

ACKNOWLEDGMENTS

We thank I. I. Fabrikant, T. J. Gay, D. H. Jaecks, and A. F. Starace for illuminating discussions and we acknowledge the support of the National Science Foundation, Grant No. PHY-9109164.

[1] J. A. R. Samson, in *Photoionization and Other Probes of Many-Electron Interactions*, edited by F. J. Wuilleumier (Plenum, New York, 1975), pp. 419–430.

[2] U. Fano and J. W. Cooper, Rev. Mod. Phys. **40**, 441 (1968).

[3] E. Matthias, P. Zoller, D. S. Elliot, N. D. Piltch, S. J. Smith, and G. Leuchs, Phys. Rev. Lett. **50**, 1914 (1983).

[4] S. Edelstein, M. Lambropoulos, J. Duncanson, and R. S. Berry, Phys. Rev. A **9**, 2459 (1974); J. A. Duncanson, Jr., M. P. Strand, A. Lindgard, and R. S. Berry, Phys. Rev. Lett. **37**, 987 (1976).

[5] M. P. Strand, J. Hanson, R.-L. Chien, and R. S. Berry, Chem. Phys. Lett. **59**, 205 (1978); J. C. Hanson, J. A. Duncanson, Jr., R.-L. Chien, and R. S. Berry, Phys. Rev. A **21**, 222 (1980); R.-L. Chien, O. C. Mullins, and R. S. Berry, *ibid*. **28**, 2078 (1983).

[6] V. Lange, U. Eichmann, and W. Sandner, Phys. Rev. A **44**, 4737 (1991); K. Bartschat, B. M. McLaughlin, and R. A. Hoversten, J. Phys. B **24**, 3359 (1991); L.-W. He, C. E. Burkhardt, M. Ciocca, J. J. Leventhal, and S. T. Manson, Phys. Rev. Lett. **67**, 2131 (1991); R. P. Wood, C. H. Greene, and D. Armstrong, Phys. Rev. A **47**, 229 (1993).

[7] D. J. Armstrong, R. P. Wood, and C. H. Greene, Phys. Rev. A **47**, 1981 (1993).

[8] D. J. Armstrong and F. Robicheaux, Phys. Rev. A **48**, 4450 (1993).

[9] M. Pahler, C. Lorenz, E. v. Raven, J. Ruder, B. Sonntag, S. Baier, B. R. Muller, M. Schulze, H. Staiger, P. Zimmermann, and N. M. Kabachnik, Phys. Rev. Lett. **68**, 2285 (1992); S. Baier, M. Schulze, H. Staiger, P. Zimmermann, C. Lorenz, M. Pahler, J. Ruder, B. Sonntag, J. T. Costello, and L. Kiernan, J. Phys. B **27**, 1341 (1994).

[10] D. Dill, Phys. Rev. A **7**, 1976 (1973); D. Feldmann, G. Otto, D. Petring, and K. H. Welge, J. Phys. B **19**, L141 (1986).

[11] J. A. R. Samson and J. L. Gardner, Phys. Rev. Lett. **31**, 1327 (1973); Y. Morioka, M. Watanabe, T. Akahori, A. Yagishita, and M. Nakamura, J. Phys. B **18**, 71 (1985); J. S. Keller, J. E.

Hunter III, and R. S. Berry, Phys. Rev. A **43**, 2270 (1991).
[12] M. D. Lindsay, L.-T. Cai, G. W. Schinn, C.-J. Dai, and T. F. Gallagher, Phys. Rev. A **45**, 231 (1992); M. D. Lindsay, C.-J. Dai, L.-T. Cai, T. F. Gallagher, F. Robicheaux, and C. H. Greene, *ibid*. **46**, 3789 (1992).
[13] V. Lange, U. Eichmann, and W. Sandner, J. Phys. B **22**, L245 (1989).
[14] M. Aymar and J. M. Lecomte, J. Phys. B **22**, 223 (1989).
[15] V. Lange, M. Aymar, U. Eichmann, and W. Sandner, J. Phys. B **24**, 91 (1991).
[16] B. Rouvellou, J.-M. Bizau, D. Cubaynes, J. Novak, M. Pahler, L. Journel, F. J. Wuilleumier, L. Voky, P. Faucher, A. Hibbert, and N. Berrah, Phys. Rev. Lett. **75**, 33 (1995).
[17] K. W. McLaughlin, D. S. Eschliman, O. P. Francis, and D. W. Duquette, Phys. Rev. A **49**, 240 (1994).
[18] J. Sugar and C. Corliss, J. Phys. Chem. Ref. Data Suppl. 2 **14**, 51 (1985).
[19] K. W. McLaughlin and D. W. Duquette, J. Opt. Soc. Am. B **9**, 1953 (1992).
[20] N. F. Ramsey, *Molecular Beams* (Oxford University Press, London, 1956), p. 14, Eq. II.9.
[21] A. Fischer and I. V. Hertel, Z. Phys. A **304**, 103 (1982).
[22] J. R. Taylor, *An Introduction to Error Analysis* (University Science, Mill Valley, CA, 1982).
[23] J. M. Chambers, *Computational Methods for Data Analysis* (Wiley, New York, 1977), pp. 149–151; J. E. Dennis, in *The State of the Art in Numerical Analysis*, edited by D. Jacobs (Academic, London, 1977), pp. 269–306.
[24] G. Leuchs and S. J. Smith, J. Phys. B **15**, 1051 (1982).
[25] S. Baier, A. N. Grum-Grzhimailo, and N. M. Kabachnik, J. Phys. B **27**, 3363 (1994).
[26] N. M. Kabachnik and I. P. Sazhina, J. Phys. B **9**, 1681 (1976).
[27] K. W. McLaughlin, Ph.D. thesis, University of Nebraska, 1995.
[28] A. F. Starace, in *Handbuch der Physik*, edited by W. Mehlhorn (Springer-Verlag, Berlin, 1982), Vol. 31.
[29] O. C. Mullins, R.-L. Chien, J. E. Hunter III, J. S. Keller, and R. S. Berry, Phys. Rev. A **31**, 321 (1985).